Source-mask optimization (SMO): from theory to practice

Thuc Dam*[a], Vikram Tolani[a], Peter Hu[a], Ki-Ho Baik[a], Linyong Pang[a], and Bob Gleason[a]
Steven D. Slonaker[b] and Jacek K. Tyminski[b]
[a]Luminescent Technologies, Inc., 2471 East Bayshore Road, Palo Alto, CA, USA 94303;
[b]Nikon Precision Inc, 1399 Shoreway Road, Belmont, CA, USA 94002-4107

ABSTRACT

Source Mask Optimization techniques are gaining increasing attention as RET computational lithography techniques in sub-32nm design nodes. However, practical use of this technique requires careful considerations in the use of the obtained pixilated or composite source and mask solutions, along with accurate modeling of mask, resist, and optics, including scanner scalar and vector aberrations as part of the optimization process. We present here a theory-to-practice case of applying ILT-based SMO on 22nm design patterns.

Keywords: SMO, ILT, OPC, optical aberrations, scanner aberrations, Zernike aberrations, Jones pupil aberrations

1. INTRODUCTION

Aberrations induce edge placement errors that contribute to variation in sizes and displacement of patterns. Although advanced projection optics have very small aberrations, requirements for total CD control and overlay approaching 2 nm make it important to consider any single component that might contribute as little as 0.5 nm to a CD or overlay budget. Standard practices in common use cover some of the effects of aberrations. OPC models calibrated using SEM measurements of printed patterns easily capture the effects of aberrations on line widths, but aberrations may make it invalid to assume that the measured line widths correspond to equal and opposite deviations of edges from a target. A model based on this invalid assumption will not predict pattern placement properly, and may not extrapolate well to patterns outside its calibration data set. If masks or illuminators are designed to improve depth of focus in addition to putting nominal images on target, performance with respect to aberrations that have certain similarity to defocus will also improve. Any order of spherical aberration or astigmatism is in this class. On the other hand, improving performance in the presence of an asymmetric aberration, such as coma, may require explicit consideration of the aberration during optimization.

The work reported here covers optimization of an illuminator and masks to print a set of test patterns in the presence of either scalar aberrations, represented as a Zernike expansion, or vector aberrations, represented as a Jones pupil. Although it would be instructive to consider the effects of single aberrations, we chose to use sets of many small aberrations because no modern lithographic lens design has significant single aberrations. The aberrations we used do not correspond to an actual scanner. We chose values that are larger than those of real designs because we wanted to explore the limits to which mask and illuminator design can mitigate the effects of aberrations. For the same reason, we did not constrain complexity of mask patterns. Trade-off between lithographic performance and simplification of mask patterns to reduce manufacturing cost is an important topic, but imposing such constraints on the optimization would interfere with our objective of exploring the limits of what is possible in the presence of aberrations. The cases we compare include optimizing both the illuminator and the mask with explicit treatment of aberrations, neglecting aberrations while optimizing the illuminator but including them while optimizing the mask, and neglecting them while optimizing both the illuminator and the mask.

2. EXPERIMENTAL AND RESULTS

2.1 Experimental Setup

The patterns selected for this work are dark-field arrays of square apertures, each of which is well-suited to quadrupole illumination if optimized individually without aberrations. Some perform better if the poles are along the x and y axes, and others if they are rotated by 45°, and the optimum pole locations vary with pattern pitch. The illuminator obtained

when images of the patterns are optimized collectively is therefore a compromise. Some of the arrays have 90° rotational symmetry. Others have only 180° symmetry, although effects of departure from 4-fold rotational symmetry are mostly confined to shapes near the corners of the arrays. Based on the symmetry of the layouts, we expect that a parametric representation of the illuminator as a pair of quadrupoles will give good results for the unaberrated optimization. Because aberrations can introduce additional asymmetry into the problem, we chose to represent the illuminator as four pairs of dipoles, the lowest illumination symmetry that would not de-center an image out of focus. The SMO algorithm was sequential, alternating between adjusting the illuminator and mask to minimize the same objective function. Details of the method used for mask optimization are published elsewhere. [1,2] Because our objective was to study optical phenomena, we did not use a model for a particular resist in this work, and simply applied a constant threshold to the bulk intensity in the resist film to calculate locations of pattern edges.

Table 2.11 describes the matrix of source mask optimization (SMO) experiments. The parametric SMO experiments consist of two components 1) source and 2) mask optimizations. The source optimization employed is a bounded parametric optimization whereby source parameters inner/outer sigma, fan open angles, and fan intensities are varied. The initial source consists of 4 independent dipoles as depicted in Figure 2.11. The objective function to be optimized includes nominal, -50 nm defocus, and +/- 1 nm mask biased images, each with equal weight. The mask is allowed to be free-form curvilinear with mask rule check (MRC) turned off, consistent with our objectives to investigate the limits of unconstrained optimization. As depicted in table 2.11, SMO was conducted with and without XY polarization, Jones pupil aberrations, and Zernike aberrations. We did not cover the dependence of aberrations on field coordinates in this work because such exhaustive characterization of projection optics is not generally available. Treating the field dependence properly would also involve averaging across the scanning direction, which is unnecessary here because we treat only mean aberrations averaged over the field. Variables in the optimization also included photoresist threshold.

	SMO Conducted with		
	No Aberations	JonesPupil	Zernike
No Polarization	SMO-NN	SMO-JN	SMO-ZN
XY Polarization	SMO-NP	SMO-JP	SMO-ZP

Table 2.11. SMO experiments.

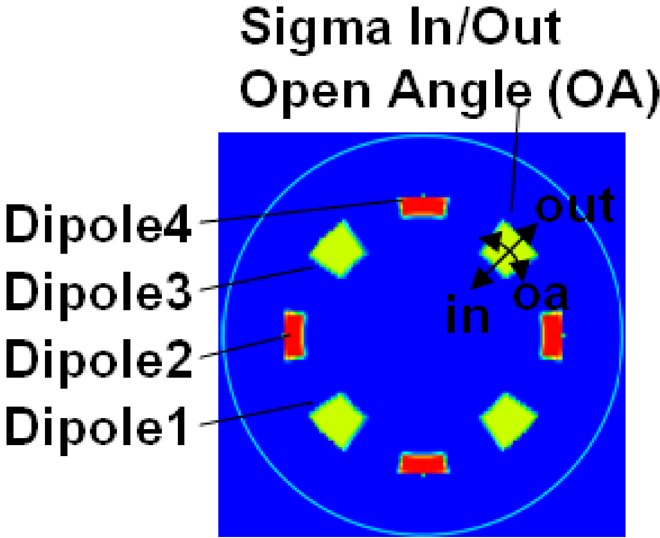

Figure 2.11. Source parameters being varied by parametric optimizer.

Other fixed setup parameters are:

NA = 1.3
Resist Filmstack = Typical 193nm resist setup with matched substrate.

Image/Focal Plane = top of film stack
Vector optical model

The following list contains the variables in the optimization, their initial values, and bounds (in brackets).

Dipoles 1 and 3
- Sigma In = 0.5 [0, 0.7]
- Sigma Out = 0.9 [0.7, 1]
- Open Angle = 20° [0 ,40°]
- Starting Angle = 45° & 135° [Fixed]
- Fan Intensity = 0.7 [0, 1]

Dipoles 2 and 4
- Sigma In = 0.6 [0, 0.7]
- Sigma Out = 0.8 [0.7, 1]
- Open Angle = 20° [0 ,40°]
- Starting Angle = 0 & 90 [Fixed]
- Fan Intensity = 1 [0, 1]

Photoresist Threshold = 0.24

Input target patterns used for SMO are described in Figure 2.12. Each pattern has equal weight in the SMO cost function with the pattern region for optimization being focused on line-ends. Pattern corners are not considered in the optimization.

The collected litho performance metrics are line ends edge placement errors (EPE), mask error enhancement factor at +/- 1 nm mask bias (MEEF), and process variation band between images at 0, +50 nm, and -50 nm defocus at 100% dose (PV-band).

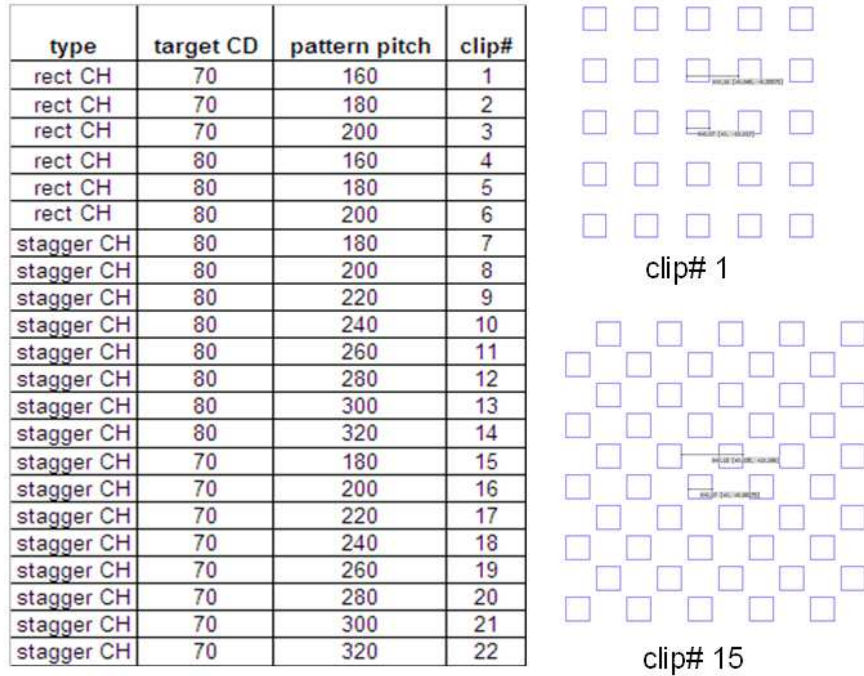

type	target CD	pattern pitch	clip#
rect CH	70	160	1
rect CH	70	180	2
rect CH	70	200	3
rect CH	80	160	4
rect CH	80	180	5
rect CH	80	200	6
stagger CH	80	180	7
stagger CH	80	200	8
stagger CH	80	220	9
stagger CH	80	240	10
stagger CH	80	260	11
stagger CH	80	280	12
stagger CH	80	300	13
stagger CH	80	320	14
stagger CH	70	180	15
stagger CH	70	200	16
stagger CH	70	220	17
stagger CH	70	240	18
stagger CH	70	260	19
stagger CH	70	280	20
stagger CH	70	300	21
stagger CH	70	320	22

Figure 2.12. SMO target patterns used for multi-clip optimization.

In the first set of SMO experiments, no aberrations are included during the optimization. The source and masks obtained will be referred to as SMO-NN_{src} and SMO-NN_{msk}. The experiment is repeated with XY polarization, and this source mask combination will be referred to as SMO-NP_{src} and SMO-NP_{msk}. The forward simulations for these masks and sources are collected, and are considered the ideal results without any aberrations used in either optimizations or forward simulations. In practice scanners, however, do have aberrations, which if unaccounted during SMO optimization could

lead to undesirable images during print or simulations. To assess these unaccounted aberrations, the SMO-NN & -NP masks are forward simulated with Jones pupil and Zernike aberrations added to the SMO-NN(P)$_{src}$, and these simulated results will be referred to as SMO-NN(P)$_{msk\text{-}fwdJP}$ and SMO-NN(P)$_{msk\text{-}fwdZern}$. To assess whether mask optimization alone can correct for these unaccounted aberrations, ILT mask optimization was conducted using SMO-NN(P)$_{src}$ with Jones pupil and Zernike aberrations included in the forward simulation engine. These masks and simulated results will be referred to as SMO-NN(P)$_{msk\text{-}ILT\&fwdJP}$ and SMO-NN(P)$_{msk\text{-}ILT\&fwdZern}$.

In the second set of SMO experiments, Jones pupil aberrations are included during the optimization. The source and masks obtained will be referred to as SMO-JN$_{src}$ and SMO-JN$_{msk}$. The experiment is repeated with XY polarization, and this source combination will be referred to as SMO-JP$_{src}$ and -JP$_{msk}$.

In the third set of SMO experiments, Zernike aberrations are included during the optimization. The source and masks obtained will be referred to as SMO-ZN$_{src}$ and SMO-ZN$_{msk}$. The experiment is repeated with XY polarization, and this source combination will be referred to as SMO-ZP$_{src}$ and -ZP$_{msk}$.

2.2 Results

Figure 2.13 shows the sources that were obtained at the end of each SMO experiment.

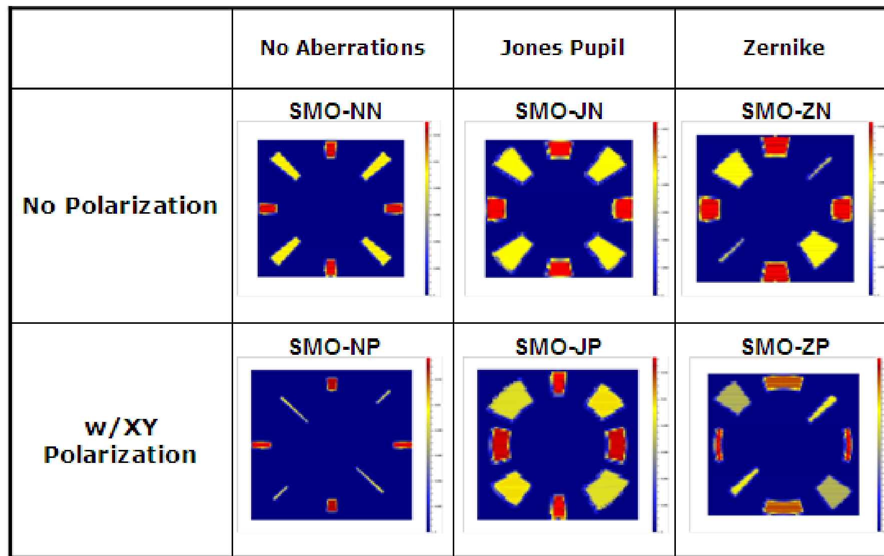

Figure 2.13 Parametric SMO sources obtained from 3 experiments with different aberrations and polarization.

The sources obtained with unaberrated light shows high degree of symmetry and coherent fans. With inclusion of Jones pupil aberrations into SMO, the sources have more asymmetric fans with wider open angles. As Zernike aberrations are applied, the 45° dipole fans shrink significantly and increases the asymmetry in the SMO source.

We selected clip 2 in this study to illustrate how these aberrations affect SMO solutions and their images. The mask and images generated from the first SMO experiments (SMO-NN$_{src}$ and SMO-NN$_{msk}$) are shown in Figure 2.14. Note the absence of perfect four-fold rotational symmetry in these solutions, even though this clip has a four-fold axis. This is due to the illuminator not having exact four-fold symmetry due to its joint optimization with other patterns, such as clip 15 in Figure 2.12. As is discussed below, this degree of asymmetry is small compared to that induced by the aberrations, so it has no effect on our conclusions. In this figure, the green images are generated by simulating the blue masks at nominal and +/50 nm defocus conditions without any aberrations. As one can see, the nominal image converged to the red square target, while the + and – 50 nm defocus images (right side) are smaller than target by ~3 nm. Both defocus images are nearly on top of each other indicating that defocus asymmetry is insignificant.

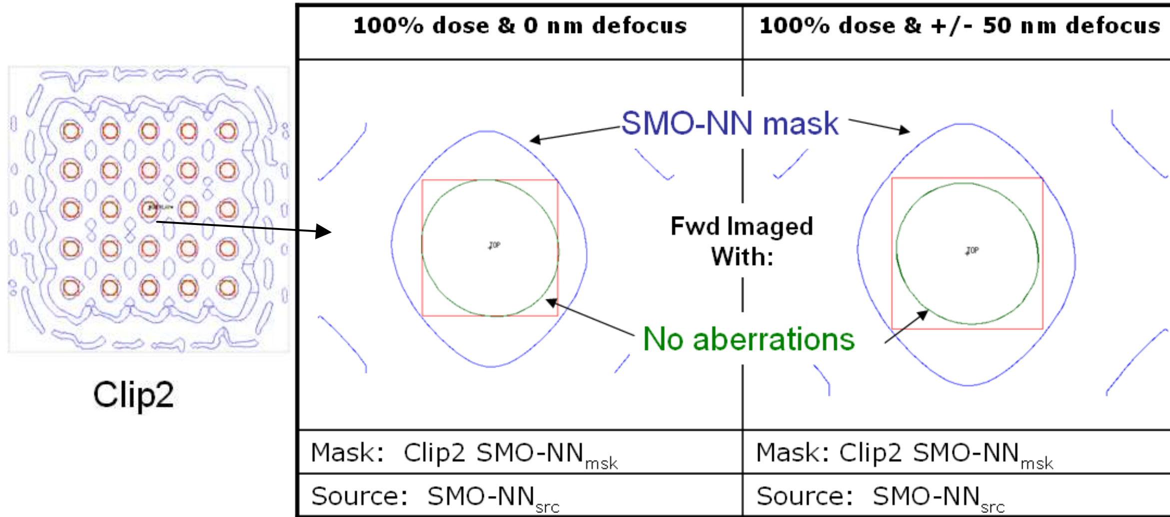

Figure 2.14. Clip2 SMO-NN$_{msk}$ simulated with SMO-NN$_{src}$ without aberrations at nominal and +/- 50 nm defocus.

When Jones pupil aberrations are applied during simulation with SMO-NN$_{src}$ and SMO-NN$_{msk}$ (Figure 2.15), the red nominal and defocus images are smaller than the green, unaberrated images.

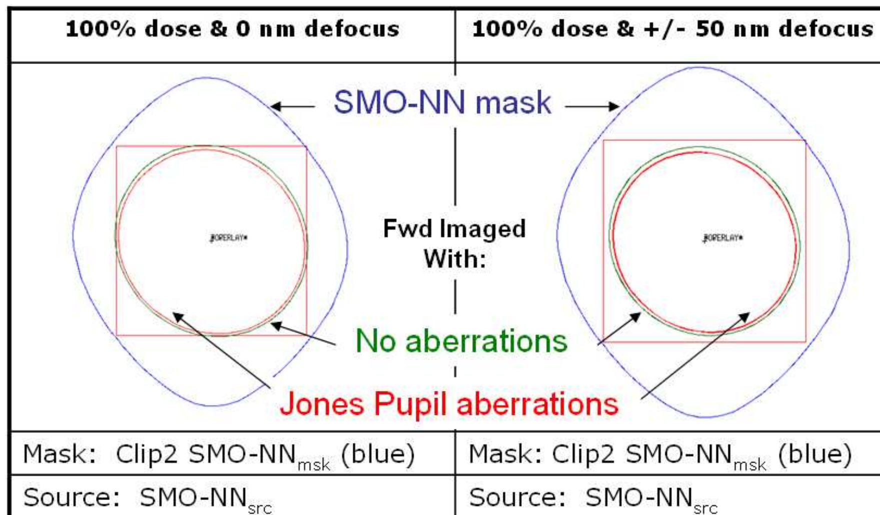

Figure 2.15. Clip2 SMO-NN$_{msk}$ simulated with SMO-NN$_{src}$ with Jones pupil aberration at nominal and +/- 50 nm defocus.

When Zernike aberrations are applied during simulation with SMO-NN$_{src}$ and SMO-NN$_{msk}$ (Figure 2.16), the red nominal and defocus images are shifted 9-10 nm to the right of the green, unaberrated images. The two defocus images (-/+ 50 nm) become asymmetric in defocus and are separated by ~3 nm, where as the green defocus images are nearly on top of one another.

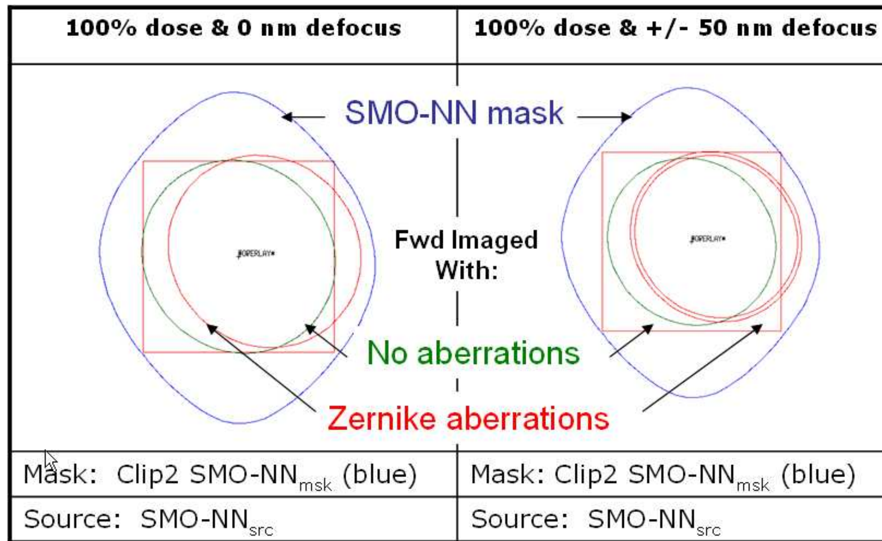

Figure 2.16. Clip2 SMO-NN_{msk} simulated with SMO-NN_{src} with Zernike aberration at nominal and +/- 50 nm defocus.

The overall data for the first experiment is summarized for all clips and imaging conditions in Figure 2.17. This result shows the Zernike aberrations affected image quality the most. It shows large EPE deviation (9-10 nm) and larger PV bands for all 22 clips, most of which as demonstrated in the clip2 simulated images are due to lateral image shift. Jones pupil aberrations also show minor EPE & PV shift. Neither aberration affects MEEF very much, and XY polarized light tends to contribute to PV band improvements (Figure 2.17c).

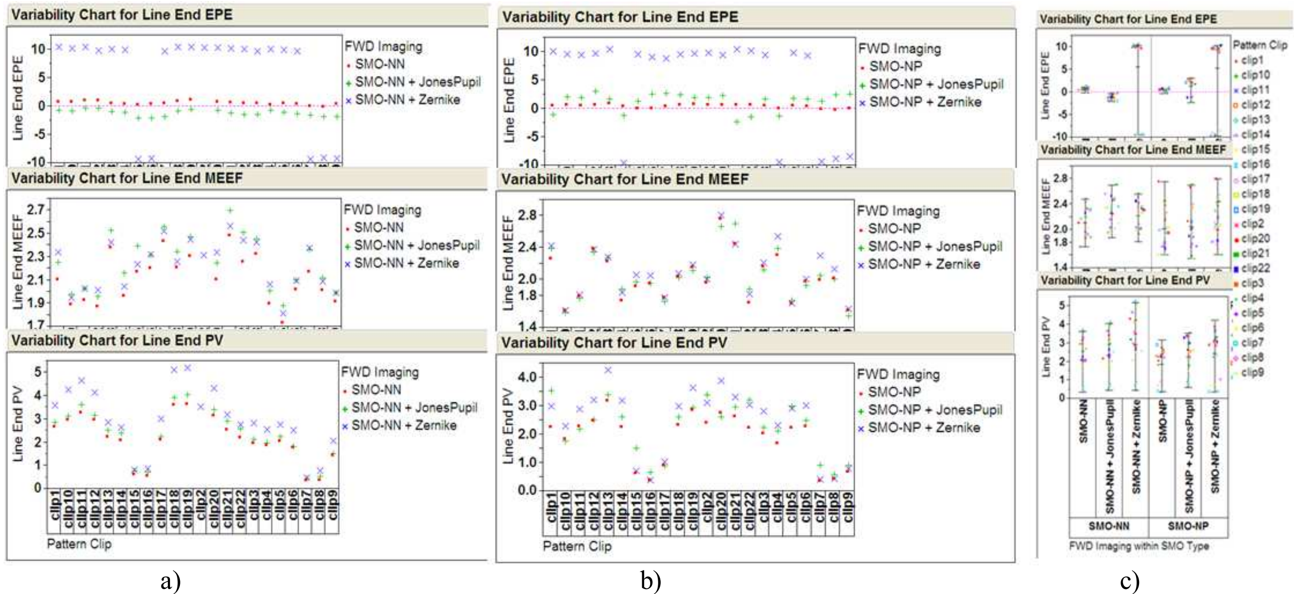

Figure 2.17. a) SMO-NN's line end EPE, MEEF, and PV results. b) SMO-NP's line end EPE, MEEF, and PV results. c) comparison plot between SMO-NN & SMO-NP results.

After documenting the lithographic effects of Jones pupil and Zernike aberrations, we considered two possible ways to mitigate them. One approach is to include aberrations only when optimizing the mask, using the source obtained from the SMO solution without aberrations. The other is to include the aberrations in all SMO steps. In continuation of the first SMO experiment, SMO-NN_{src} is used during mask inversion for clip 2 with aberration. In Figure 2.18, SMO-NN_{src} is used for inversion with Jones pupil aberration. The resulting blue mask (SMO-$NN_{msk\text{-}ILT\&fwdJP}$) is slightly larger than

SMO-NN$_{msk}$, and the comparison of the simulated images showed that the blue image contours are converged to the red square target. This indicates that the Jones pupil effects of image shrinkage can be mitigated with mask correction alone.

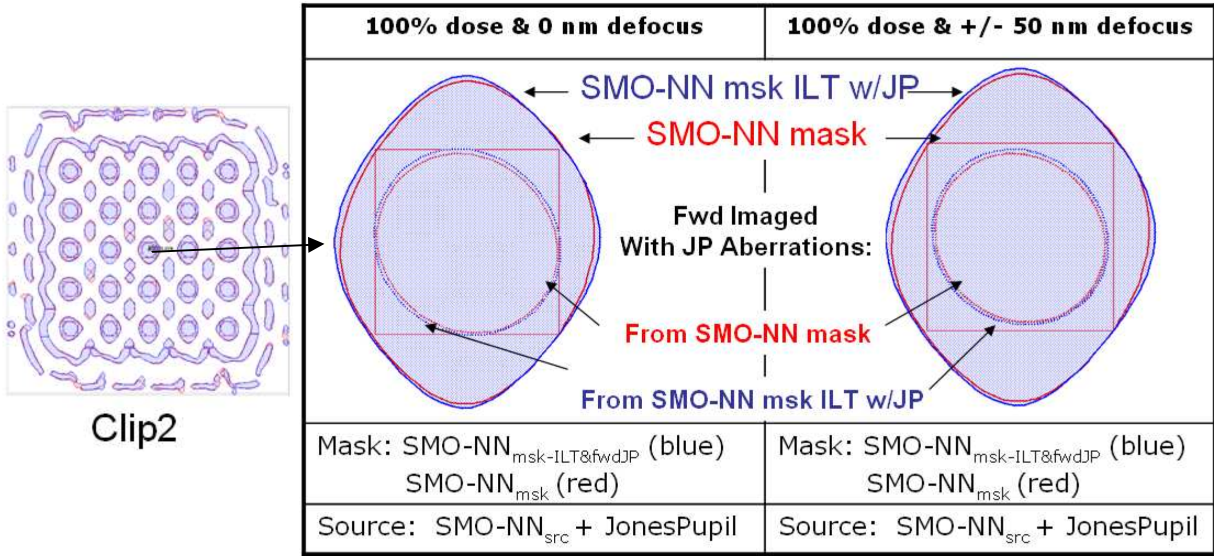

Figure 2.18. With a fixed SMO-NNsrc, mask inversion with Jones pupil can correct image shrinkage caused by Jones pupil aberration.

In Figure 2.19, SMO-NN$_{src}$ is used for inversion with Zernike aberration for clip 2. The resulting blue mask (SMO-NN $_{msk-ILT\&fwdZern}$) is shifted to the left compared to SMO-NN$_{msk}$. The simulated images showed that the blue nominal image contour is better converged to the red square target. This indicates that the Zernike effects of lateral image shift can be mitigated with mask correction. The defocus image contours are also better centered, but the defocus asymmetry between +50 nm and -50 nm defocus remains uncorrectable by mask optimization.

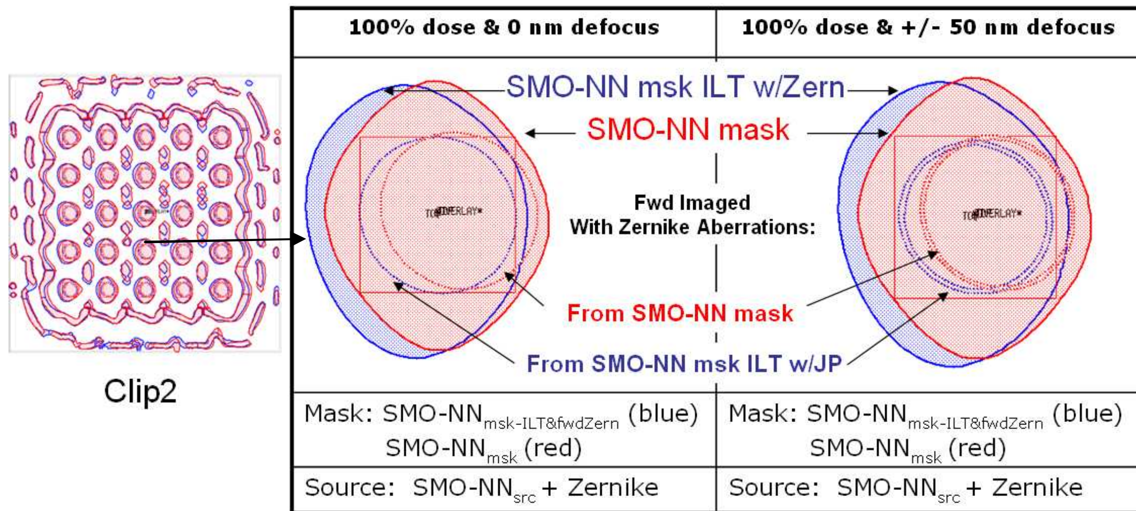

Figure 2.19. With a fixed SMO-NNsrc, mask inversion with Zernike can correct image shift caused by Zernike aberration, but does not seem to be able to correct for the defocus asymmetry.

Figure 2.20 summarizes all the lithographic performance data for mask inversion studies. In general, this data shows that mask inversion with aberrations can correct for the image shift and shrinkage caused by Zernike and Jones pupil aberrations, respectively, without any impact on MEEF. There, however, remains a gap in PV band performance that

cannot be recovered by mask inversion alone with the Zernike aberrations. XY polarized light improves PV band performance when Zernike aberrations are present for the conditions and patterns in this study. (Figure 2.20c).

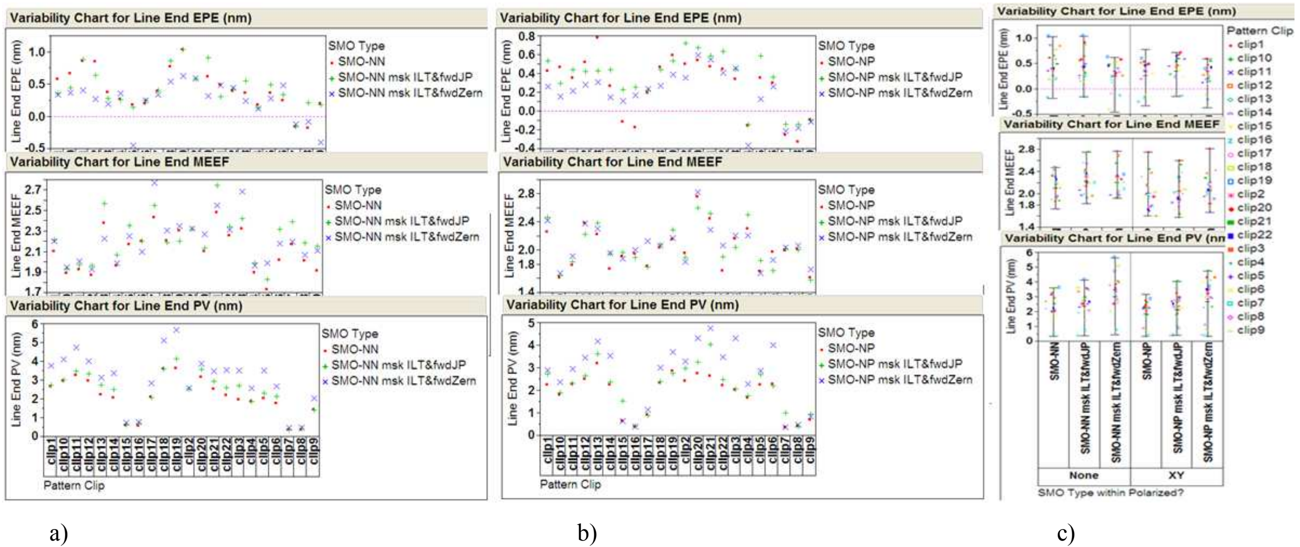

Figure 2.20. a) SMO-NN's line end EPE, MEEF, and PV results for mask inversion that includes aberrations. b) SMO-NP's line end EPE, MEEF, and PV results for mask inversion that includes aberrations. c) comparison plot between polarized and unpolarized results.

In the second set of SMO experiments, Jones pupil aberrations are included in each step of the optimization. The resulting clip2 SMO-JN_{msk} and simulated images are shown in Figure 2.21. Relative to the SMO-NN_{msk}, SMO-JN_{msk} is larger, and its resulting simulated images are converged for nominal and are well matched at defocus. It would appear that SMO with Jones pupil accounted for during optimization can result in images that have comparable performance to ideal case.

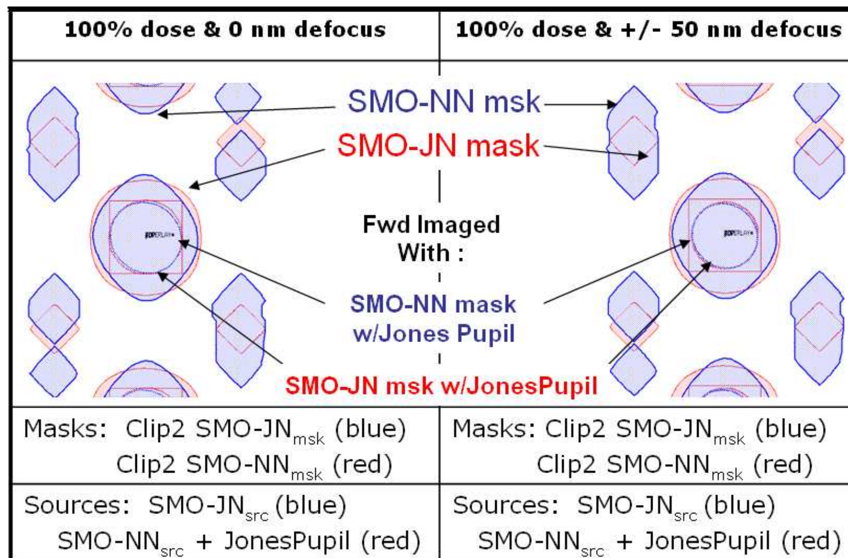

Figure 2.21. Clip 2 SMO-JN_{msk} and simulated images.

In the third set of SMO experiments, Zernike aberrations are included in each step of the optimization. The clip 2 mask SMO-ZN_{msk} and simulated images are displayed in Figure 2.22. The blue SMO-ZN_{msk} is correcting for the Zernike aberration by shifting to the left as was also seen in the mask-only optimization. The other interesting change is the

different SMO-ZN$_{msk}$'s SRAF, which occurred mostly likely due to difference in the source. Image centering and targeting are close to those of the unaberrated results in Figure 2.14, although differences between contours corresponding to positive and negative defocus values are not completely eliminated by including the aberrations in the SMO solution.

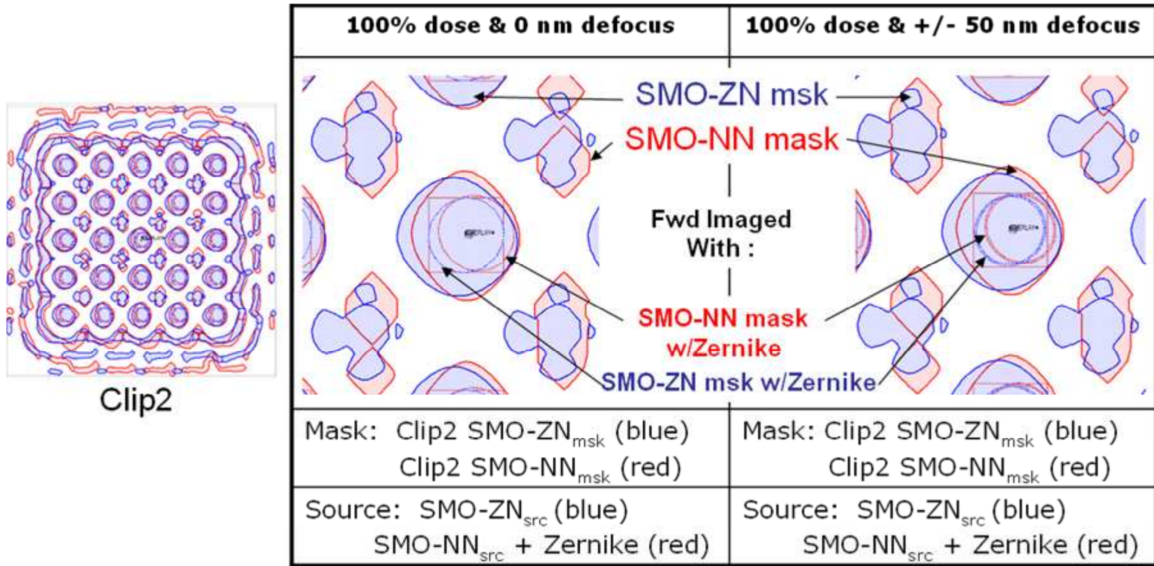

Figure 2.22. Clip 2 SMO-ZN$_{msk}$ and simulated images.

The compilation of litho performance metric for SMO conducted with Jones pupil and Zernike aberrations are summarized in Figure 2.23. This data indicates that SMO with aberrations can lead to converged images (EPE close to 1 nm for all cases), and very little impact on MEEF. PV is best for the unaberrated case, while the Zernike aberrations appear difficult to correct, most likely due to the asymmetry in defocus images. XY polarization had little effect on SMO conducted with aberrations for the patterns in this study.

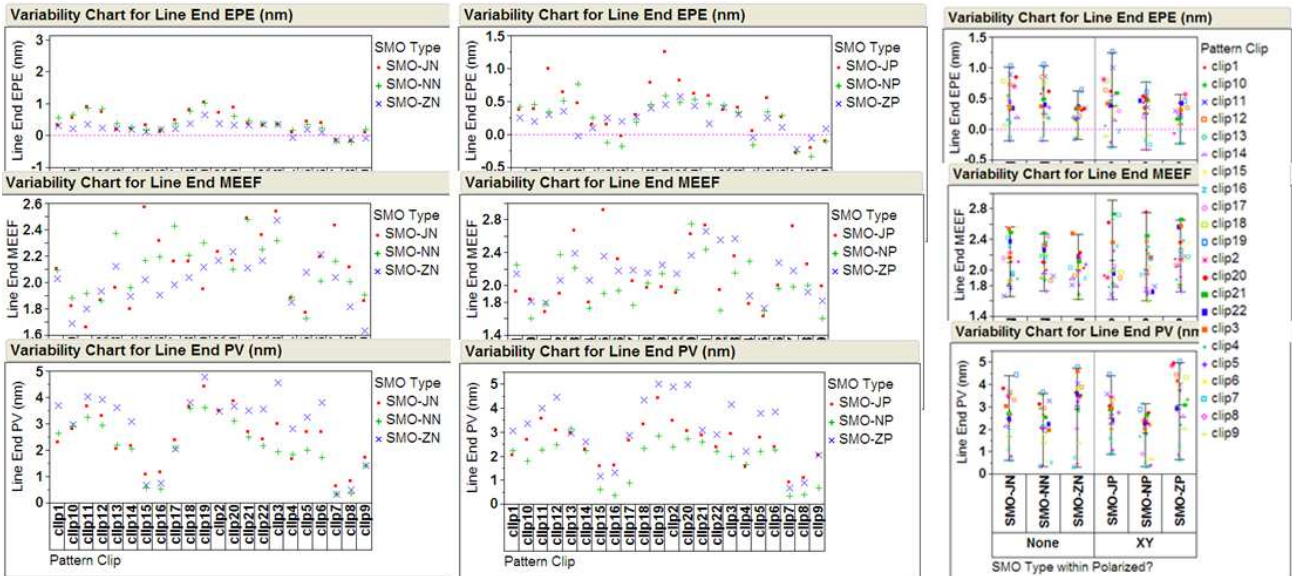

a) b) c)

Figure 2.23. a) Line end EPE, MEEF, and PV results from SMO with aberrations included and with unpolarized light. b) Line end EPE, MEEF, and PV results from SMO's with aberrations included and with XY polarized light. . c) comparison plot between XY polarized and unpolarized results

3. DISCUSSIONS & CONCLUSION

Accounting for aberrations during each step of the SMO process can produce solutions whose lithographic performance is close to that of the ideal unaberrated case, even with aberrations that are larger than those of any modern projection optics. For the types of patterns in this study, dark-field arrays of square apertures, the dominant effects of aberrations showed in nominal image fidelity and depth of focus. MEEF performance was a much less sensitive indicator. We observed improvement in image quality for both scalar and vector aberrations, and for unpolarized and polarized illumination. Although the scalar aberrations we chose to study showed poorer lithographic performance than the vector aberrations, this was simply due to the presence of a large image shift that happened to be in the Zernike coefficients, and says nothing about the relative importance of using the Jones pupil formalism to cover dependence of aberrations on polarization. One of the most important conclusions from this work is that even with such a large aberration, which shifts and distorts the nominal image contour, we obtain good solutions both in and out of focus by properly accounting for it during SMO. This aberration is a good example of one that affects both overlay and CD variation. Even if it were practical to calibrate an OPC model using measurements of individual edge positions rather than CDs in an attempt to account for pattern displacements, it would be impossible to determine whether the displacement of this particular pattern was due to simple distortion (pattern-independent) or an aberration such as coma (pattern-dependent), solely from measurements performed on its image. This is why explicit treatment of aberrations in the SMO process provides better extrapolation outside of the patterns in the calibration data set, and better prediction of off-nominal image properties. These considerations will become more important as we push total budgets for overlay and CD control down to the 2 nm level.

REFERENCES

[1] Daniel Abrams and Lingyong Pang, Fast Inverse Lithography Technology, Proceedings of the S.P.I.E. 6154-55, 2006

[2] Daniel Abrams, Danping Peng, and Stanley Osher, Method or Time-Evolving Rectilinear Contours Representing Photo Masks, U.S. Patent 7,124,394, 2006